Effects of Optical-Density and Phase Dispersion of an Imperfect Band-Limited Occulting Mask on the Broadband Performance of a TPF Coronagraph

Erkin Sidick* and Kunjithapatham Balasubramanian
Jet Propulsion Laboratory, California Institute of Technology, 4800 Oak Grove Drive, Pasadena, CA, USA 91109

ABSTRACT

Practical image-plane occulting masks required by high-contrast imaging systems such as the TPF-Coronagraph introduce phase errors into the transmitting beam, or, equivalently, diffracts the residual starlight into the area of the final image plane used for detecting exo-planets. Our group at JPL has recently proposed spatially profiled metal masks that can be designed to have zero parasitic phase at the center wavelength of the incoming broadband light with small amounts of OD and phase dispersions at other wavelengths. Work is currently underway to design, fabricate and characterize such image-plane masks. In order to gain some understanding on the behaviors of these new imperfect band-limited occulting masks and clarify how such masks utilizing different metals or alloys compare with each other, we carried out some modeling and simulations on the contrast performance of the high-contrast imaging testbed (HCIT) at JPL. In this paper we describe the details of our simulations and present our results.

Keywords: TPF, integrated modeling, speckle-nulling, high-contrast coronagraph

1. INTRODUCTION

One of the key components of TPF-Coronagraph is an image-plane occulting mask located in an intermediate image plane. It is used to block the incoming starlight while allowing planet light to pass through to the final image plane. Kuchner and Traub have shown that a conventional coronagraph with an ideal band-limited graded image-plane mask can, in principle, provide an arbitrarily large dynamic range without need for phase control or a severe Lyot stop **[1]**. However, as far as we know, no one has made or described a process to make a focal plane occulting mask that is phase-free. Our group at Jet Propulsion Laboratory (JPL), California Institute of Technology, has successfully designed, fabricated and tested a type of occulting mask, a gray-scale pattern written in high-energy beam sensitive (HEBS) glass using a high-voltage electron-beam lithography facility at JPL **[2]**. It is a linear (or one-dimensional) mask, designed with a Sinc^2 function of a single variable, x. It has been found that this type of occulting mask displays an optical-density (OD) and wavelength dependent parasitic phase, and its OD profile also changes with wavelength **[2-3]**. Our studies conducted on this type of occulting mask by evaluating the broadband contrast performance of the High-Contrast Imaging Testbed (HCIT) at JPL **[4-5]** have predicted that it is difficult, if not impossible, to achieve a broadband contrast C_m=C_4=1x10^{-9} or better using such a mask **[6-9]**. Here, C_m is the mean contrast and C_4 is a contrast at an angular separation of 4λ/D, and the broadband contrast is the one obtained with a broadband light source centered at around λ_0 = 785nm wavelength and having a bandwidth, $\Delta\lambda$=0.1λ_0. However, the ultimate goal of TPF-Coronagraph is to achieve broadband contrast values of C_m=C_4=1x10^{-10} or better in the visible and near infrared spectrum to observe faint planets orbiting the nearby starts.

Recently, Balasubramanian *et al.* proposed several spatially profiled metal masks (SPMM's) as an alternative solution for high-contrast broadband coronagraph **[10-11]**. Work is currently underway at JPL to design, fabricate and test this type of occulting mask **[12]**. We have conducted preliminary studies on these new mask designs through modeling and simulations and derived the requirements on their OD and phase dispersions when the broadband contrast targets range from 1x10^{-9} to 1x10^{-10} **[13]**. Different materials pose different levels of difficulty when fabricating such SPMM's. Also, one has a choice to apply or not to apply a profiled dielectric layer on the front or back side to correct the monochromatic phase profile, i.e., to neutralize transmitted phase versus OD across the mask at the center wavelength of the desired band **[11]**. Adding such a dielectric layer may yield better contrast values, but it also adds extra burden to the

*Erkin.Sidick@jpl.nasa.gov; Phone 1 818 393-7585; Fax 1 818 393-9471; www.jpl.nasa.gov

fabrication process of the mask and causes more fabrication errors. Therefore, it is necessary to understand the differences in the behaviors of the various mask designs to make an informed decision on the choice of material. It is also very important to understand the trade-off between having and not-having the extra profiled dielectric layer before selecting a mask design. This paper addresses the following issues: (i) The difference in the behaviors of the SPMM's using different materials, and (ii) the role of an extra spatially profiled dielectric layer in improving the broadband contrast performance of a Lyot coronagraph. We conduct our investigation by evaluating the contrast performance of the HCIT through modeling and simulations. The HCIT is a full Lyot coronagraph with all the features of the planned TPF-C instrument. However, it suffers from an amplitude-drooping effect in the pupil caused by the artificial star.. As described in Ref. [6], our simulation tool allows us to turn-on or off this effect in the simulation. We have found that, when taking into account the HEBS glass occulter's phase and the surface errors of all other optics in the simulation of the HCIT, turning on or off such an amplitude-drooping effect makes only negligible difference in the obtainable contrast floor. Therefore, we do not take into account this effect in this paper. As to the measured surface errors of all optical components on the HCIT, we present our results obtained by both accounting for and not accounting for those errors. The independently measured surface errors of the HCIT optics have already been reported in Ref. [6] and that description will not be repeated here.

2. BRIEF DESCRIPTION OF THE HCIT

In this section, we briefly describe the HCIT's optical system and components. The schematic diagram of the HCIT layout in the *xz*-plane is shown in Figure 1. Artificial starlight is created by a 5μm pinhole illuminated by an optical

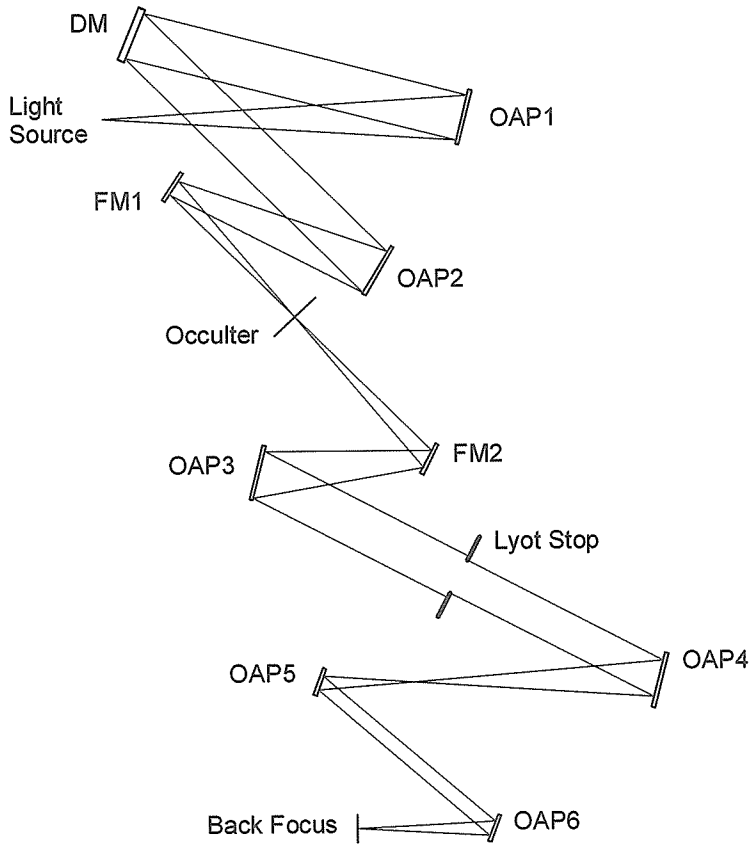

Figure 1. Schematic diagram of the High Contrast Imaging Testbed layout. The light source ("starlight") is a 5μm pinhole illuminated by an optical fiber, and a CCD science camera is located at the back focal plane for detecting the image of the "starlight".

fiber. An off-axis parabolic mirror (OAP1) collimates the light from the pinhole and directs it to a high-density, 32x32 actuator deformable mirror (DM), which performs wavefront control. A circular aperture mask on the DM defines the system pupil of the HCIT, and has a diameter of D=30mm. After the DM, the collimated light is re-imaged onto the focal plane of the occulting mask by OAP2 and a flat-mirror (FM1). The occulting mask attenuates the starlight, and almost has no effect on the light of a planet if present. The "back-end" of the system, from the occulting mask to the back focus plane, supports experimentation with diverse coronagraph configurations and apodizations. A flat mirror (FM2) and OAP3 re-collimate the light passing through the occulter mask and form a same-size sharp image of the DM pupil at the Lyot plane. A Lyot stop blocks the ring-like residual light diffracted off the occulting mask while letting most of the planet light through. After OAP4 forms an image from the remaining stellar and planet lights, it is then magnified ($M \approx 3$) by the OPA5-OAP6 pair for proper sampling on the CCD science camera located at the back focal plane. More information on the HCIT and the DM can be found in Refs. **[4-5]**.

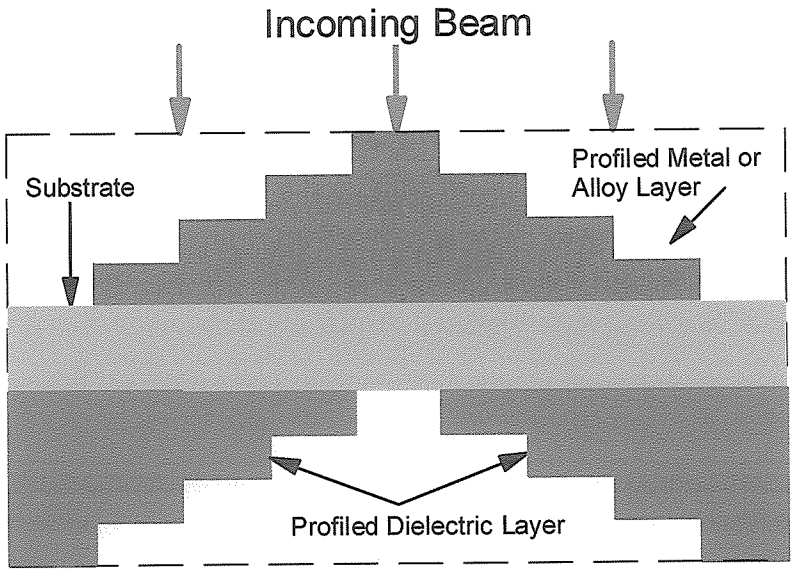

Figure 2. Schematic diagram of a conceptual spatially profiled metal or alloy mask. The geometric steps are exaggerated for clarity and are not to scale. There can be a thin anti-reflection layer on top of the metal layer, or a thin uniform metal or dielectric layer between the metal layer and the dielectric substrate. When the mask does not have a phase-compensating spatially profiled dielectric layer, it is referred to as an "uncorrected" mask. Usually the substrate consists of a Fused Silica or a BK7 slab, and a PMMA layer is assumed for the profiled dielectric layer in this paper.

3. SPATIALLY PROFILED METAL MASKS

The schematic diagram of a spatially profiled metal mask (SPMM) is shown in **Fig. 2**. The metal or alloy layer provides the desired OD profile, and the profiled dielectric layer is added to cancel the wavefront phase error that the metal layer introduces to the transmitting beam at its center wavelength, λ_0. We assume Fused Silica for the substrate, and PMMA for the spatially profiled dielectric layer in this paper. When a mask does not have a profiled dielectric layer, we call it an "uncompensated mask". Real masks can be a little more sophisticated that what is shown in Fig. 2. For example, an anti-reflection (AR) dielectric coating layer can be added on top of the metal layer to minimize the reflection of the incoming beam. Or a uniform thin dielectric or metal under-layer can be sandwiched between the metal layer and the substrate **[11]**.

Reference **[11]** described the general issues related to the design and fabrication of SPMM's, and presented the OD and the phase properties of four SPMM designs. Three of them consist of metals, namely, Pt, Ni, and Cr, and the other one consists of an alloy, namely, Inconel. The variation of OD with wavelength is comparable for Ni, Pt and Inconel films, but is worse for Cr. The phase versus thickness curves of Ni and Inconel films are comparable and have the smallest slopes, and that of Cr has the largest one. The slope of the similar curve for Pt lies between the above two slope values.

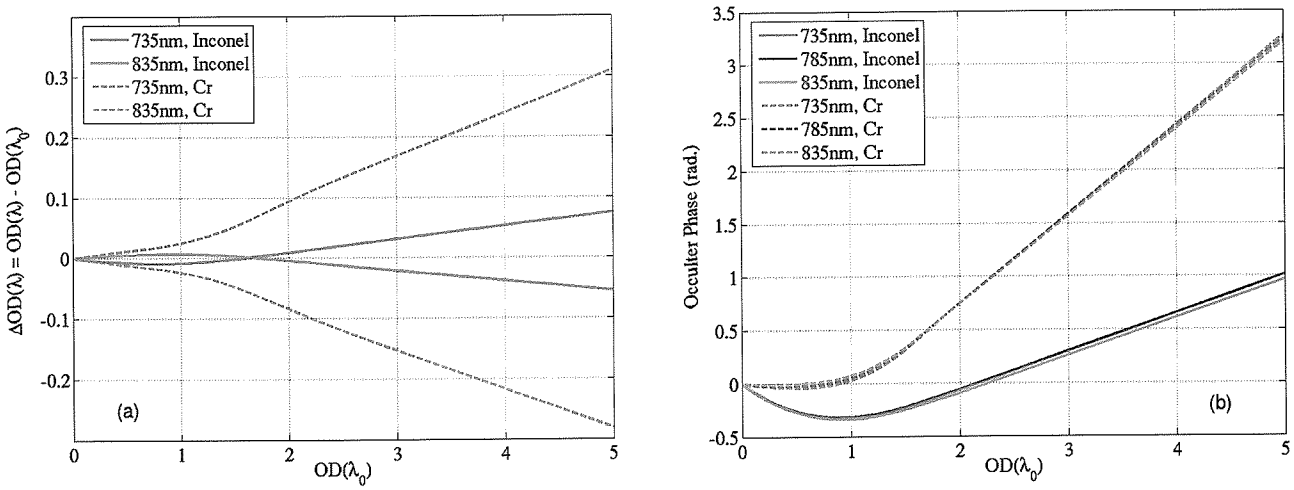

Figure 3. Variations of (a) the differential OD and (b) phase-delay of two uncorrected occulting masks as a function of $OD(\lambda_0)$ with wavelength as a parameter. One mask consists of Inconel, and the other of Cr, respectively, as indicated in the figure legends. These results are similar to those shown in Fig. 9 (OD) and Fig. 10 (phase) of Ref. [11] for Inconel and Cr. The signs of the occulting mask phases are reversed in part (b) because this figure shows the phase-delay of the corresponding occulter versus $OD\lambda_0$), but the similar plots in Ref. [11] show the "phase advance". In these figures, the wavelengths $\lambda = 735$nm and $\lambda = 835$nm correspond to $\lambda = \lambda_0 \pm 50$nm, the extreme wavelength components of a beam having a bandwidth of $\Delta\lambda = 100$nm and centered at $\lambda_0 = 785$nm.

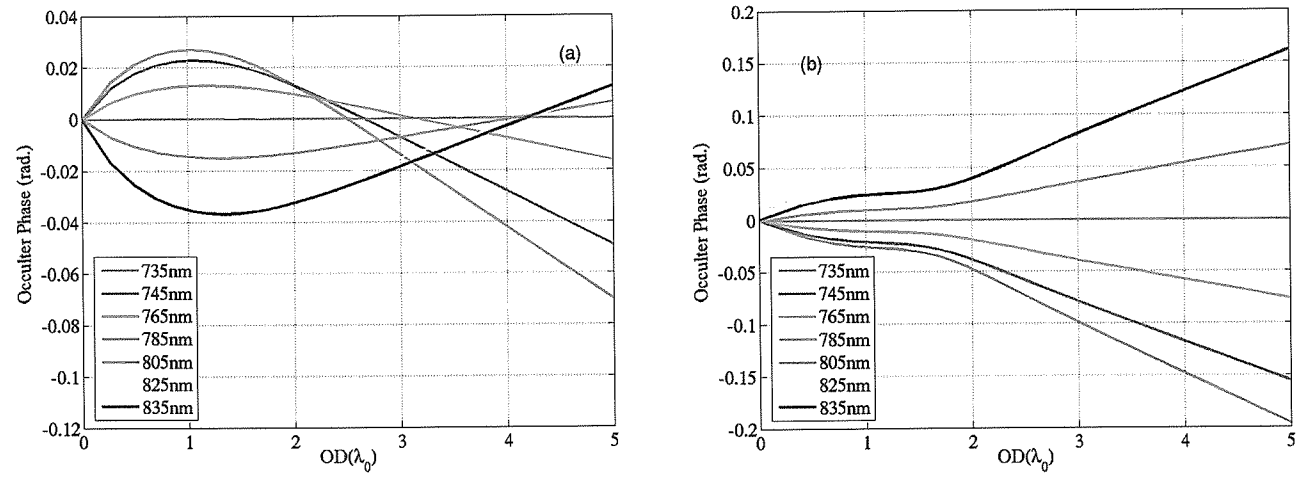

Figure 4. Phase-delay versus $OD(\lambda_0)$ obtained for a PMMA-corrected occulting mask with wavelength as a parameter. (a) Inconel on Fused Silica, and (b) Cr on Fused Silica. $\lambda_0 = 785$nm.

Therefore, we will only examine the behaviors of an Inconel and a Cr masks in this paper. The behaviors of the masks consisting of the remaining two as well as other similar materials can be estimated based on the results predicted for the Inconel and the Cr masks.

Figures 3(a) and **3(b)** show the variations of the differential OD, $\Delta OD(\lambda)$, and the phase profiles of uncorrected Inconel and Cr masks as a function of $OD(\lambda_0)$. In part (a), only the values of $\Delta OD(\lambda)$ at the wavelengths $\lambda = 735$nm and $\lambda = 835$nm are shown. These wavelength values correspond to the extreme wavelength components in the passband of a beam having a bandwidth of $\Delta\lambda = 100$nm and centered at $\lambda_0 = 785$nm. In part (b), in addition to the above two λ values,

the phase values at λ_0 = 785nm are also included. If these two masks are corrected with a spatially profiled PMMA layer, then their OD profiles (Fig. 3(a)) stay almost unchanged, but the phase curves changed to those shown in **Figs. 4(a)** and **4(b)** for the Inconel and the Cr masks, respectively. In this case, the occulter phase becomes fully corrected at $\lambda = \lambda_0$ = 785nm, but remains as non-zero with small non-zero values at other wavelengths. That is, these two occulters have small amounts of OD and phase dispersions.

In this paper, we assume continuous curves for the OD and the phase profiles of the SPMM's. This is a good approximation when such a mask is fabricated with adequate accuracy and with a small enough step size. The intensity transmittance of an SPMM is assumed to be described by

$$T(x) = \left[1 - \left(\frac{\sin(\pi x / w)}{(\pi x / w)}\right)^2\right]^2, \qquad (1)$$

when $\lambda = \lambda_0$, where w is the occulter width parameter. Its values at other wavelengths as well as its wavelength-dependent phases are determined from the optical properties of the corresponding mask material and geometry as shown in Figs. 3 and 4. **Figure 5** shows the OD and the phase profiles of an Inconel mask. Part (a) is the OD profile at $\lambda = \lambda_0$, part (b) are the phase profiles of an uncorrected mask at three wavelengths, and part (c) is the same as part (b) except this is for a PMMA-corrected mask. **Figure 6** shows the same data for a Cr mask. These two figures (Figs. 5 and 6) are plotted with the same scale for comparison.

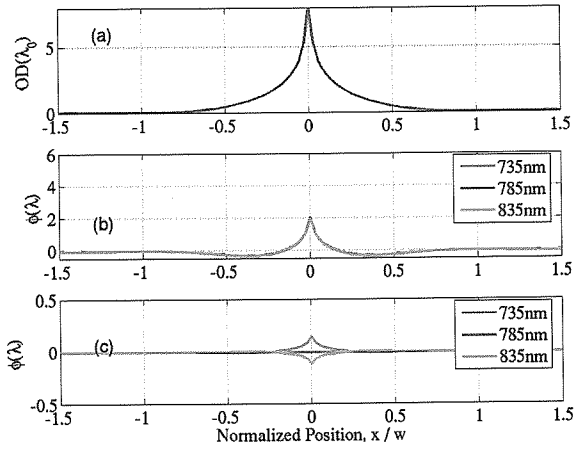

Figure 5. Variation of the OD and the phase of an Inconel occulter as a function of position. w is the occulter width parameter. (a) OD, (b) phase of the uncorrected occulter, and (c) phase of a PMMA-corrected occulter. λ_0 = 785nm.

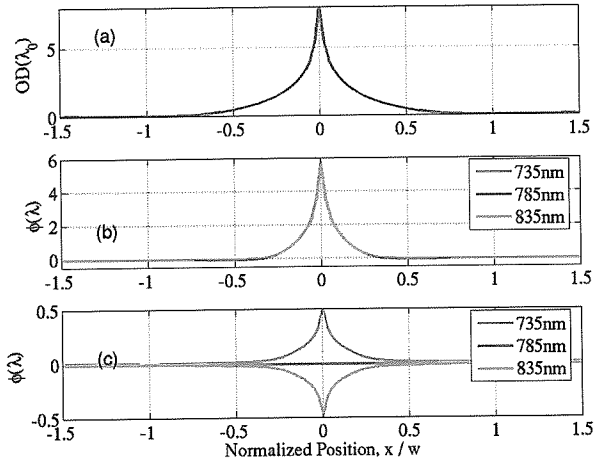

Figure 6. Same as Fig. (5) except this figure is for a Cr occulter.

4. SIMULATION RESULTS

In this section, we describe our results on the contrast simulations of the HCIT. In all of our simulations, we assumed w = 144μm and ε = 0.40D (Lyot stop parameter).

4.1 Uncorrected Masks

Monochromatic behavior of an occulting mask can be predicted by looking at the contrast floor that one can achieve in a Lyot coronagraph system. When we carried out numerical speckle-nulling optimization on the HCIT's optical model by assuming an Inconel and a Cr masks, respectively, we obtain the results for C_m as shown in **Figs. 7(a)** and **7(b)**. Each

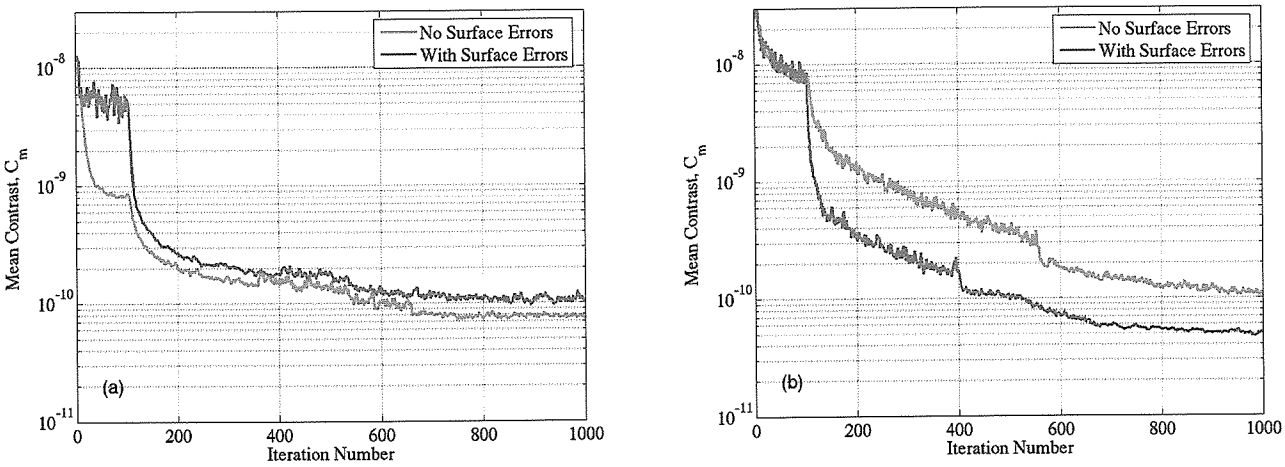

Figure 7. Predicted monochromatic C_m values at $\lambda_0 = 785$nm versus speckle-nulling iteration number corresponding to the two cases shown in the figure legend, where "Surface Errors" means the measured surface errors of all optics used on the HCIT. (a) Uncorrected Inconel mask, and (b) uncorrected Cr mask. In all cases, speckle-nulling was carried out in the right-half plane in the interval of Iteration = 1 to 100, in the [*X*min *X*max *Y*min *Y*max] = [3 11 -11 11]*λ/D window in the interval of Iteration = 101 to about 500, and in the [4 10 -10 10]*λ/D after that, where *X* and *Y* are the position variables in the final focal plane normalized by the corresponding focal distance. Abrupt changes in C_m curves in other places occurred when the speckle-nulling gain parameter was adjusted.

curve in these figures depicts the C_m values as a function of speckle-nulling iteration number. The causes for abrupt changes in C_m values seen in these figures are explained in the figure caption. One important point to note from these results is that when the phase-delay of an occulter is relatively small, such as the case of the Inconel occulter in Fig. 7(a), including the surface errors of all optics on the HCIT worsens the monochromatic C_m floor. However, when the phase-delay of an occulter is relatively large, the surface errors of all optics can improve the achievable monochromatic contrast performance of the system, as seen in Fig. 7(b). When a coronagraph is free of all errors except the occulter phase, it diffracts the residual light into the fairly regular rings of speckles in the final image plane, as shown in **Figs. 8(a)** and **8(c)**, where the simulated point-spread function (PSF) of the HCIT using a Cr occulter is shown for two speckle-nulling steps. One is before conducting any speckle-nulling and the other is after 1000 iterations of speckle-nulling. The surface errors in the coronagraph system randomize the pattern of the diffracted speckles as shown in Figs. **8(b)** and **8(d)**, and make the job of the DM more efficient as compared to the case where there is no any surface error.

If we evaluate the broadband performance of the HCIT using the monochromatic DM phase solutions at Iteration = 1000 in Figs. 7(a) and 7(b), we obtain **Figs. 9(a)** and **9(b)** for the cases of Inconel and Cr masks, respectively. The procedure for simulating the broadband contrast performance of the HCIT is described in Ref. [9]. As expected, the Inconel occulter yields better broadband contrast performance as compared to the Cr occulter due to Inconel's weaker OD and phase dispersions. Also, the surface errors of all optics degrade the broadband C_m slightly in both cases, but in the case of Inconel occulter, they lead to a better broadband C_4 value, just as in the case of a monochromatic light. The C_m and C_4 values at $\Delta\lambda = 0$ (monochromatic) and $\Delta\lambda = 0.1\lambda_0$ are summarized in **Table 1**.

4.2 Corrected Masks

The Inconel and Cr masks whose phase profiles are corrected at $\lambda = \lambda_0$ with a spatially profiled PMMA layer possess OD and phase dispersion characteristics as shown in Fig. 3(a) and Figs. 4(a) and 4(b), respectively. Because the phases of these masks are ideally zero at $\lambda = \lambda_0$, it is not necessary to carry out a speckle-nulling optimization when the HCIT is free of any other surface error. Our simulation has predicted that an error-free HCIT has the monochromatic contrast floors of $C_m = 1.65\text{x}10^{-14}$ and $C_4 = 3.76\text{x}10^{-15}$, respectively [13]. When the HCIT utilizes such a PMMA-corrected occulter, the occulter's OD and phase dispersions will come into play when the input beam is a broadband light and degrades the HCIT's broadband contrast performance. The predicted broadband contrast values of the HCIT when

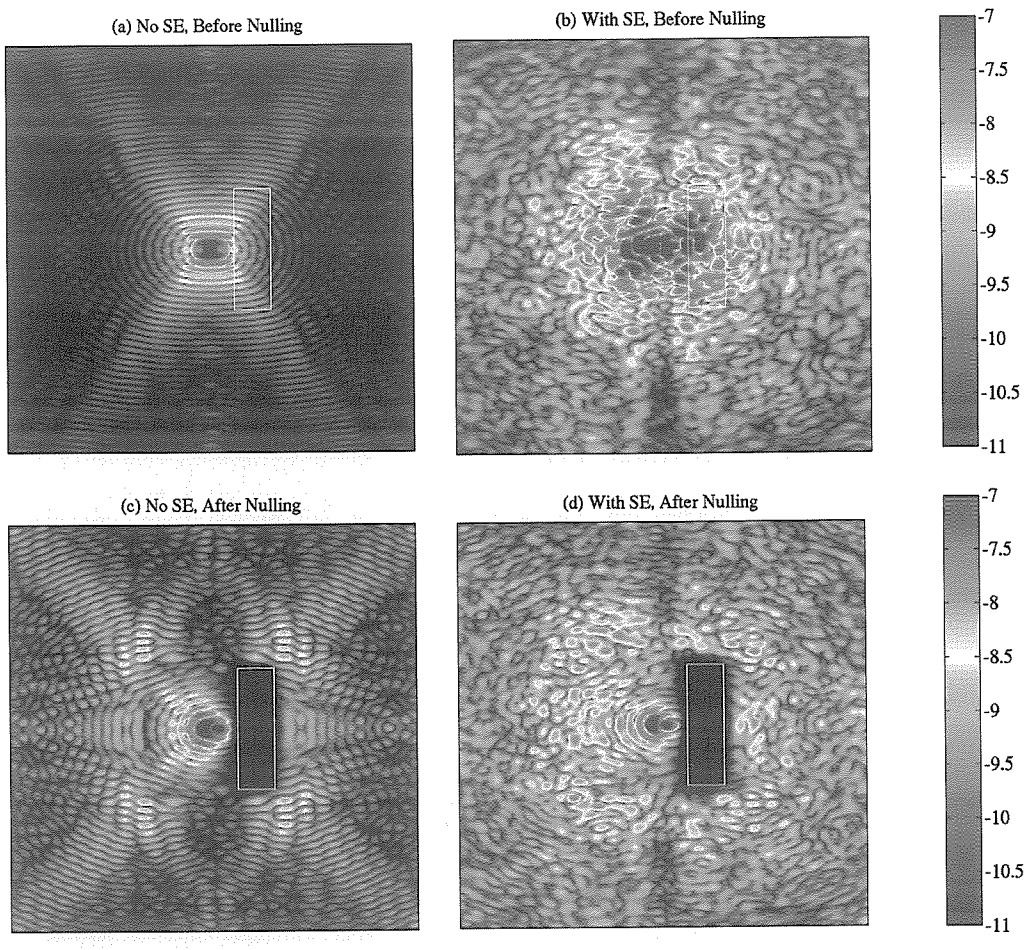

Figure 8. Predicted monochromatic PSF in the final image plane of the HCIT utilizing a Cr mask. The white rectangular box in each part corresponds to the field angle area of the "half-dark hole", or [4 10 -10 10] *λ/D. "With SE" means the simulation takes into account the surface errors of all optics, and "No SE" means the simulation does not include them. In each case of "After Nulling", the corresponding DM phase solution at Iteration = 1000 in Fig. 7 is applied to the DM when calculating the PSF.

Table 1. Summary of monochromatic and the $\Delta\lambda = 0.1\lambda_0$ (10%) broadband results of C_m and C_4 obtained in Section 4. In all cases, w = 144μm. "Occ. Phase" means occulter phase, "Phase Disp." the phase dispersion of the occulter, and "Surf. Errors" the measured surface errors of all optics.

Case #	Mask	Occ. Phase	Phase Disp.	Surf. Errors	$\Delta\lambda = 0$ (Monochromatic)		$\Delta\lambda = 0.1\lambda_0$		Fig. #
					C_m	C_4	C_m	C_4	
1.1	Inconel	X	X		7.24×10^{-11}	3.08×10^{-10}	1.05×10^{-9}	4.71×10^{-9}	9(a)
1.2	Inconel	X	X	X	9.90×10^{-11}	2.32×10^{-10}	1.59×10^{-9}	3.56×10^{-9}	9(a)
2.1	Cr	X			1.07×10^{-10}	3.20×10^{-10}	6.33×10^{-9}	4.44×10^{-8}	9(b)
2.2	Cr	X	X	X	4.71×10^{-11}	9.67×10^{-11}	1.05×10^{-8}	6.23×10^{-8}	9(b)
3.1	Inconel		X		1.62×10^{-14}	3.76×10^{-15}	8.76×10^{-11}	6.51×10^{-10}	10(a)
3.2	Inconel		X	X	5.51×10^{-11}	1.30×10^{-10}	8.57×10^{-10}	5.58×10^{-9}	10(a)
4.1	Cr		X		1.62×10^{-14}	3.76×10^{-15}	6.23×10^{-10}	5.34×10^{-9}	10(b)
4.2	Cr		X	X	5.51×10^{-11}	1.30×10^{-10}	1.30×10^{-9}	5.55×10^{-9}	10(b)
5				X	5.51×10^{-11}	1.30×10^{-10}	9.16×10^{-10}	6.88×10^{-9}	10

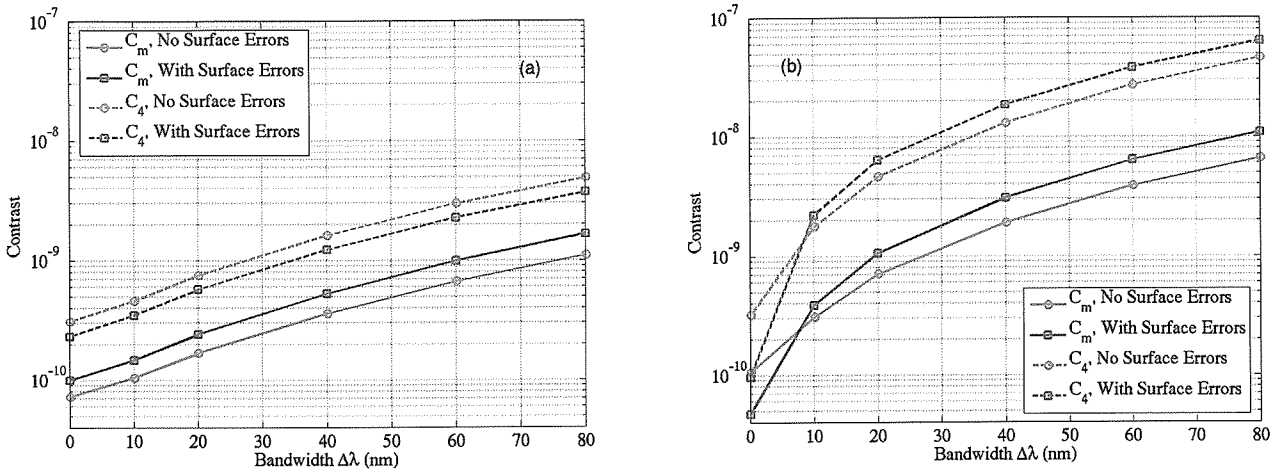

Figure 9. Predicted broadband contrast performance of the HCIT when using the DM phase solutions obtained at Iteration = 1000 in Figs. 7(a) and 7(b), respectively. (a) Inconel occulter, and (b) Cr occulter.

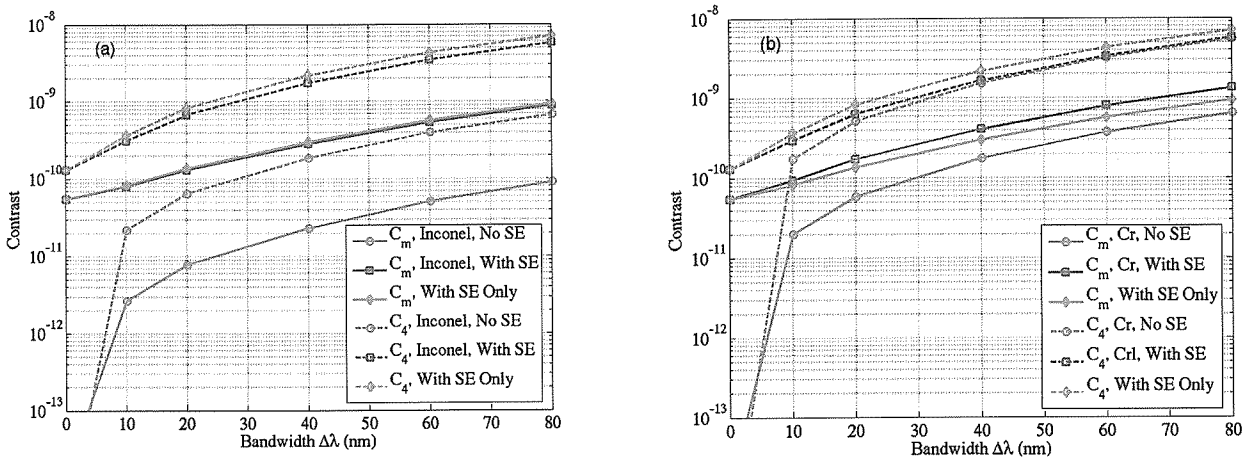

Figure 10. (a) Predicted monochromatic C_m values of the HCIT at λ_0 = 785nm versus iteration number obtained using a HEBS glass "Modified-Sinc^2" occulter with w = 144μm. In all cases, speckle-nulling was carried out in the right-half plane in the interval of Iteration = 1 to 100. Then, in the case of "SN Window Series 1", speckle-nulling was conducted in the [*X*min *X*max *Y*min *Y*max] = [3 11 -11 11]*λ/D window in the interval of Iteration = 101 to 500, and in the [4 10 -10 10]*λ/D after that, where *X* and *Y* are the position variables in the final focal plane normalized by the corresponding focal distance. In the case of "SN Window Series 2", these two SN windows are [2.5 12 -12 12]*λ/D and [4 10 -10 10]*λ/D, respectively. "SN" means "speckle-nulling". (b) Predicted broadband contrast performance of the HCIT when using the DM phase solutions obtained with Iteration = 1000 in part (a).

utilizing either the PMMA-corrected Inconel or the Cr masks are plotted in **Figs. 10(a)** and **10(b)**, respectively, as the case of "No SE", where "SE" means surface errors. In the case of Inconel occulter and there is no surface error in the HCIT, our simulation predicts $C_m = 8.76\text{x}10^{-11}$ and $C_4 = 6.51\text{x}10^{-10}$ at $\Delta\lambda = 0.1\lambda_0$ in Fig. 10(a). The corresponding values obtained with the Cr occulter in Fig. 10(b) are $C_m = 6.23\text{x}10^{-10}$ and $C_4 = 5.34\text{x}10^{-9}$, respectively. That is, these contrast values for the Inconel occulter are smaller by about an order of magnitude than those for Cr occulter. We also carried out speckle-nulling optimization for 1000 iterations on the HCIT by taking into account the surface errors of all optics as the only source of error. When we combine the surface errors of all optics and the occulter's OD and phase dispersions, and applying the monochromatic DM phase solution mentioned above, we obtained the blue curves in Figs. 10(a) and 10(b), respectively, for the Inconel and the Cr masks. In both cases of the occulting mask, the broadband contrast values increase when including the surface errors, and such an increase is more significant in the case of Inconel mask as compared to the case of Cr mask. These figures also include the contrast results of a case where the occulter's OD and

phase dispersions are ignored but the surface errors of all optics are taken into account. The results of this case (green curves) are included here for the comparison with the precious two cases. As we can see, when the HCIT optics have surface errors, the OD and the phase dispersions of the either occulting mask do not make much difference in the broadband contrast performance of the system. The surface quality of the optics currently being used on the HCIT is not good enough for achieving $C_m = C_4 = 1.0\text{x}10^{-9}$ broadband contrast values even with either the PMMA-corrected Inconel or Cr mask. The monochromatic and the broadband contrast values of the present 3 cases are also listed in Table 1.

5. CONCLUSION

We have investigated the behaviors of spatially profiled metal masks by evaluating the contrast performance of the HCIT through optical modeling and simulations. The goal was to gain some understanding on how the uncorrected and the PMMA-corrected metal or alloy masks utilizing Cr, Pt, Ni and Inconel perform in a broadband Lyot coronagraph. Considered main target application of these masks is TPF-Coronagraph. The optical properties of the above materials predicts that Inconel has the best and the Cr the worst OD and phase characteristics when used in a spatially profiled image-plane mask. Our contrast simulations of the HCIT utilizing a Cr or an Inconel mask have confirmed that Inconel mask indeed yields much better broadband C_m and C_4 values than a Cr mask in most cases considered. In the case of C_m, the difference is a factor of about 5 to 10 for the uncorrected masks and about 2 to 10 for the PMMA-corrected masks. When the surface errors of all optics on the HCIT are not taken into account, our simulations predicted that adding a PMMA-correcting layer to the Inconel and Cr masks can improve the C_m and C_4 values by a factor of 7 to 12, and such an Inconel mask yields broadband contrast values of $C_m = 8.8\text{x}10^{-11}$ and $C_4 = 6.5\text{x}10^{-10}$, respectively. Although only the Inconel and the Cr masks were treated in great detail in this paper, the results presented on these two masks can be used to estimate the behaviors of other similar masks such as Ni and Pt masks.

All of the analyses presented here use a speckle nulling algorithm to create a dark hole. There are ongoing efforts to incorporate greater a priori knowledge of the coronagraph into separate control algorithms (Energy Minimization and Electric Field Conjugation [9]), which also allow multi-wavelength optimization that are expected to yield better broadband contrast values. All of the $\Delta\lambda/\lambda = 0.1$ contrast values in Table 1, for instance, are above 10^{-9}, while simulations of alternate algorithms predict contrast below 10^{-9} for both C_m and C_4. In addition, all of the broadband contrast numbers presented here are dominated by the variations of occulter phase with wavelength inherent in HEBS glass profiles. Occulting profiles created by variable-thickness metallic coatings, for example, have very different phase behavior than HEBS, and in many cases achieve much better broadband contrasts [10-13].

We expect that the above findings will be useful in guiding the future efforts on the HCIT and other high-contrast coronagraphic imaging systems in a meaningful direction.

ACKNOWLEDGEMENTS

This work was performed at the Jet Propulsion Laboratory, California Institute of Technology, under a contract with the National Aeronautics and Space Administration.

REFERENCES

1. M. Kuchner and W. Traub, "A coronagraph with a band-limited mask for finding terrestrial planets," *Astrophys. J.*, **570**, pp. 900-908, 2002.
2. Daniel W. Wilson, Paul D. Maker, John T. Trauger, and Tony B. Hull, "Eclipse apodization: realization of occulting spots and Lyot masks," Proc. SPIE, **4860**, pp. 361-370, 2003.
3. Peter G. Halverson, Micheal Z. Ftaclas, Kunjithapatham Balasubramanian, Daniel J. Hoppe, and Daniel W. Wilson, "Measurement of wavefront phase delay and optical density in apodized coronagraphic mask materials," Proc. SPIE, **5905**, 59051I, 2005.

4. John T. Trauger, Chris Burrows, Brian Gordon, Joseph J. Green, Andrew E. Lowman, Dwight Moody, Albert F. Niessner, Fang Shi, and Daniel Wilson, "Coronagraph contrast demonstrations with the high-contrast imaging testbed," Proc. SPIE, **5487**, 1330, 2004.
5. Andrew E. Lowman, John T. Trauger, Brian Gordon, Joseph J. Green, Dwight Moody, Albert F. Niessner, and Fang Shi, "High-contrast imaging testbed for the Terrestrial Planet Finder coronagraph," Proc. SPIE, **5487**, 1246, 2004.
6. Erkin Sidick, Fang Shi, Scott Basinger, Dwight Moody, Andrew E. Lowman, Andreas C. Kuhnert, and John T. Trauger, "Performance of TPF's High-Contrast Imaging Testbed: Modeling and simulations, "Proc. SPIE, **6265**, 62653L, 2006.
7. Erkin Sidick, Andreas C. Kuhnert, and John T. Trauger, "Broadband performance of TPF's High-Contrast Imaging Testbed: Modeling and simulations, "Proc. SPIE, **6306**, 6306-32, 2006.
8. Erkin Sidick and Daniel W. Wilson, "Behavior of imperfect band-limited coronagraphic masks in a high-contrast imaging system," *Appl. Optics* **46**, pp. 1397-1407, 2007.
9. Erkin Sidick, Brian D. Kern and Andreas C. Kuhnert, "Optimizing the broadband performance of TPF's High-Contrast Imaging Testbed through modeling and simulations," Proc. SPIE, **6693**, paper 6693-49, 2007.
10. Kunjithapatham Balasubramanian, Erkin Sidick, Daniel W. Wilson, Daniel J. Hoppe, Stuart B. Shaklan, and John T. Trauger, "Band-limited masks for TPF coronagraph", *C.R. Physique*, doi:10.1016/j.crhy.2007.03.001, 2007.
11. K. Balasubramanian, "Band-limited image masks for TPF coronagraph—Materials and desings for broadband performance," submitted to *Applied. Optics*, 2007.
12. Kunjithapatham Balasubramanian, Daniel W. Wilson, Brian D. Kern, and Erkin Sidick, "Thickness-dependent optical properties of metals and alloys applicable to TPF coronagraph image masks," Proc. SPIE, **6693**, paper 6693-37, 2007.
13. Erkin Sidick, "Requirements on optical-density and phase dispersion of imperfect band-limited occulting masks in a broadband coronagraph", submitted to *Applied Optics*, 2007.